

Epitaxial synthesis of monolayer PtSe₂ single crystal on MoSe₂ with strong interlayer coupling

Zhou, Jiadong; Kong, Xianghua; Sekhar, M. Chandra; Lin, Junhao; Le Goualher, Frederic; Xu, Rui; Wang, Xiaowei; Chen, Yu; Zhou, Yao; Zhu, Chao; Lu, Wei; Liu, Fucai; Tang, Bijun; Guo, Zenglong; Zhu, Chao; Cheng, Zhihai; Yu, Ting; Suenaga, Kazu; Sun, Dong; ...Liu, Zheng

2019

Zhou, J., Kong, X., Sekhar, M. C., Lin, J., Le Goualher, F., Xu, R., Wang, X., Chen, Y., Zhou, Y., Zhu, C., Lu, W., Liu, F., Tang, B., Guo, Z., Zhu, C., Cheng, Z., Yu, T., Suenaga, K., Sun, D., ...Liu, Z. (2019). Epitaxial synthesis of monolayer PtSe₂ single crystal on MoSe₂ with strong interlayer coupling. *ACS Nano*, 13(10), 10929-10938.

<https://dx.doi.org/10.1021/acsnano.8b09479>

<https://hdl.handle.net/10356/148580>

<https://doi.org/10.1021/acsnano.8b09479>

This document is the Accepted Manuscript version of a Published Work that appeared in final form in *ACS Nano*, copyright © American Chemical Society after peer review and technical editing by the publisher. To access the final edited and published work see <https://doi.org/10.1021/acsnano.8b09479>

Downloaded on 27 Aug 2022 23:16:07 SGT

Epitaxial Synthesis of Monolayer PtSe₂ Single Crystal on MoSe₂ with Strong Interlayer Coupling

Jiadong Zhou,^{†,●} Xianghua Kong,^{‡,§,●} Chandra Mutyala,^{||,⊥,●} Junhao Lin,^{*,#} Frederic Le Goualher,[†] Rui Xu,^{§,∇} Xiaowei Wang,[†] Yu Chen,[○] Yao Zhou,[○] Chao Zhu,[†] Wei Lu,^{||,⊥} Fucai Liu,[†] Bijun Tang,[†] Zenglong Guo,[#] Chao Zhu,[†] Zhihai Cheng,^{§,∇} Ting Yu,[○] Kazu Suenaga,[◆] Dong Sun,^{*,||,⊥} Wei Ji,^{*,§} and Zheng Liu^{*,†,||}

[†]School of Materials Science and Engineering, Nanyang Technological University, 639798 Singapore

[‡]Department of Physics and Centre for the Physics of Materials, McGill University, Montreal, Quebec H3A 2T8, Canada

[§]Department of Physics and Beijing Key Laboratory of Optoelectronic Functional Materials and Micro-nano Devices, Renmin University of China, Beijing 100872, China

^{||}International Center for Quantum Materials, School of Physics, Peking University, Beijing 100871, China

[⊥]Collaborative Innovation Center of Quantum Matter, Beijing 100871, China

[#]Department of Physics, Southern University of Science and Technology, Shenzhen 518055, China

[∇]CAS Key Laboratory of Standardization and Measurement for Nanotechnology, CAS Center for Excellence in Nanoscience, National Center for Nanoscience and Technology, Beijing 100190, China

[○]Centre for Disruptive Photonic Technologies, School of Physical and Mathematical Sciences, Nanyang Technological University, 637371 Singapore

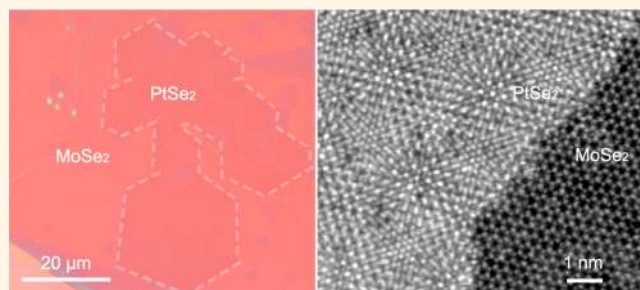
[◆]National Institute of Advanced Industrial Science and Technology (AIST), Tsukuba 305-8565, Japan

[¶]CNRS International NTU THALES Research Alliances, UMI 3288, Research Techno Plaza, 50 Nanyang Drive, Border X Block, Level 6, 637553 Singapore

S Supporting Information

ABSTRACT: PtSe₂, a layered two-dimensional transition-metal dichalcogenide (TMD), has drawn intensive attention owing to its layer-dependent band structure, high air stability, and spin-layer locking effect which can be used in various applications for next-generation optoelectronic and electronic devices or catalysis applications. However, synthesis of PtSe₂ is highly challenging due to the low chemical reactivity of Pt sources. Here, we report the chemical vapor deposition of monolayer PtSe₂ single crystals on MoSe₂. The periodic Moiré patterns from the vertically stacked heterostructure (PtSe₂/MoSe₂) are clearly identified *via* annular dark-field scanning transmission electron microscopy. First-principles calculations show a type II band alignment and reveal interface states originating from the strong–weak interlayer coupling (SWIC) between PtSe₂ and MoSe₂ monolayers, which is supported by the electrostatic force microscopy imaging. Ultrafast hole transfer between PtSe₂ and MoSe₂ monolayers is observed in the PtSe₂/MoSe₂ heterostructure, matching well with the theoretical results. Our study will shed light on the synthesis of Pt-based TMD heterostructures and boost the realization of SWIC-based optoelectronic devices.

KEYWORDS: PtSe₂, PtSe₂/MoSe₂ heterostructure, two-dimensional material, chemical vapor deposition, interlayer coupling



Platinum diselenide (PtSe₂) is an intriguing layered material due to its helical spin texture induced by local Rashba effect¹ and strong interlayer coupling.^{2,3} Recent work also revealed that the strong interlayer coupling can

Received: December 15, 2018

Accepted: September 24, 2019

Published: September 24, 2019

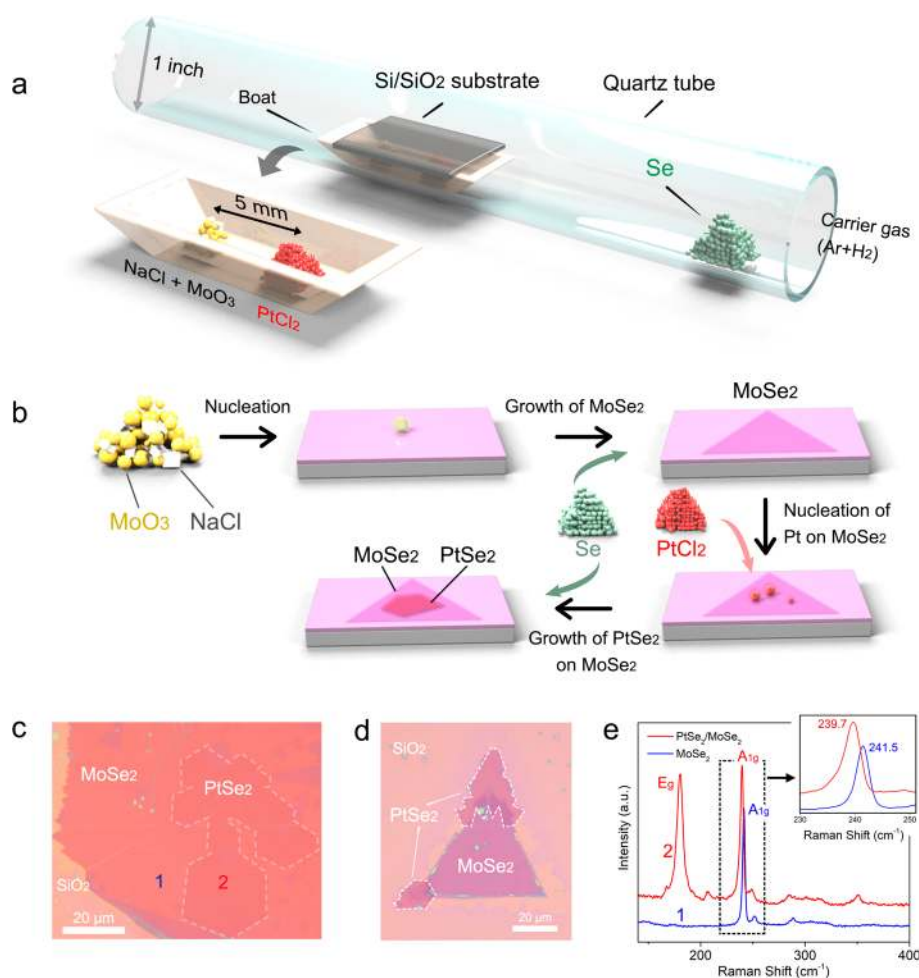


Figure 1. Reaction system and spectroscopy characterizations of PtSe₂/MoSe₂ vertical heterostructures. (a) Reaction system used to synthesize PtSe₂ and PtSe₂/MoSe₂ vertical heterostructure and the atomic crystal structure of PtSe₂/MoSe₂. (b) Growth mechanism of PtSe₂/MoSe₂ heterostructure. (c and d) Optical images of as-synthesized PtSe₂/MoSe₂ heterostructure with different styles. From the optical images, the size of the overlapped vertical heterostructure is about 40 μm, and the area of the vertical heterostructure is larger than 1000 μm². (e) The Raman spectra in the positions 1 and 2 of the heterostructure (inset shows the optical image of the vertical heterostructure). The A_{1g} mode located at 240 cm⁻¹ confirms that the crystal is MoSe₂. The Raman peaks located at 175 and 205 cm⁻¹ originate from the E_g mode of PtSe₂. The Raman peaks located at 240 cm⁻¹ can be contributed to the A_{1g} vibration mode of MoSe₂. These indicate that the as-synthesized PtSe₂ and MoSe₂ form the vertical heterostructure. Notably, the A_{1g} mode of MoSe₂ from the PtSe₂/MoSe₂ heterostructure shows a little shift due to the coupling between PtSe₂ and MoSe₂.

45 induce a PtSe₂ transition from a semimetal (bulk) to a
 46 semiconductor (monolayer) with a band gap increasing from 0
 47 to 1.2 eV.^{4,5} The narrow bandgap of few layer PtSe₂ renders it
 48 an excellent candidate for broadband mid-infrared detectors.
 49^{3,6,7} Furthermore, field-effect transistors (FETs) based on
 50 few-layer PtSe₂ display high mobility and good stability in air.⁵
 51 All these fascinating results indicate that PtSe₂ can be an
 52 attractive candidate for various applications in electronic and
 53 optoelectronic devices.⁸ Therefore, controlled synthesis of
 54 high-quality and atomically thin PtSe₂ layers is urgently
 55 required. So far, the mechanical exfoliation has been widely
 56 adopted to produce PtSe₂ monolayers. However, this method
 57 is low yield and time-consuming and usually leads to small size
 58 PtSe₂ flakes. Although few-layered PtSe₂ can be synthesized by
 59 selenization of Pt films or molecular beam epitaxy (MBE),^{9–12}
 60 synthesis of large size monolayer PtSe₂ single crystals is yet to
 61 be achieved, due to the low chemical reactivity of Pt.^{1,2,12,13}
 62 Here, we demonstrate the synthesis of monolayer PtSe₂
 63 using the chemical vapor deposition (CVD) method. Various
 64 substrates including SiO₂/Si, Al₂O₃, and MoSe₂ have been

used for the growth of PtSe₂. It is found that PtSe₂ monolayers
 65 can only be epitaxially grown on MoSe₂ substrate, forming a
 66 PtSe₂/MoSe₂ vertical heterostructure. Such structure is
 67 confirmed by the Moiré fringe from annular dark-field scanning
 68 transmission electron microscopy (ADF-STEM). First-principles
 69 calculations show that the formed heterostructure has a
 70 direct band gap and forms a type II band alignment. A more
 71 striking result lies in the emergence of interface states located
 72 within the original bandgap. These states are hybridized by the
 73 wave functions of Se-p_z and Pt/Mo-d_z² orbitals from the PtSe₂
 74 monolayer and MoSe₂ monolayer whose intrinsic interlayer
 75 couplings are strong and weak, respectively, in their own
 76 multilayers. The edge states of PtSe₂ on MoSe₂ observed with
 77 electrostatic force microscopy (EFM) compellingly support the
 78 existence of the theoretically predicted interface states. The
 79 charge transfer from PtSe₂ to MoSe₂ probed by ultrafast
 80 electron dynamics further demonstrates the interlayer coupling
 81 and band alignment in the PtSe₂/MoSe₂ heterostructure. Our
 82 work is helpful toward the synthesis of a PtSe₂ monolayer and
 83

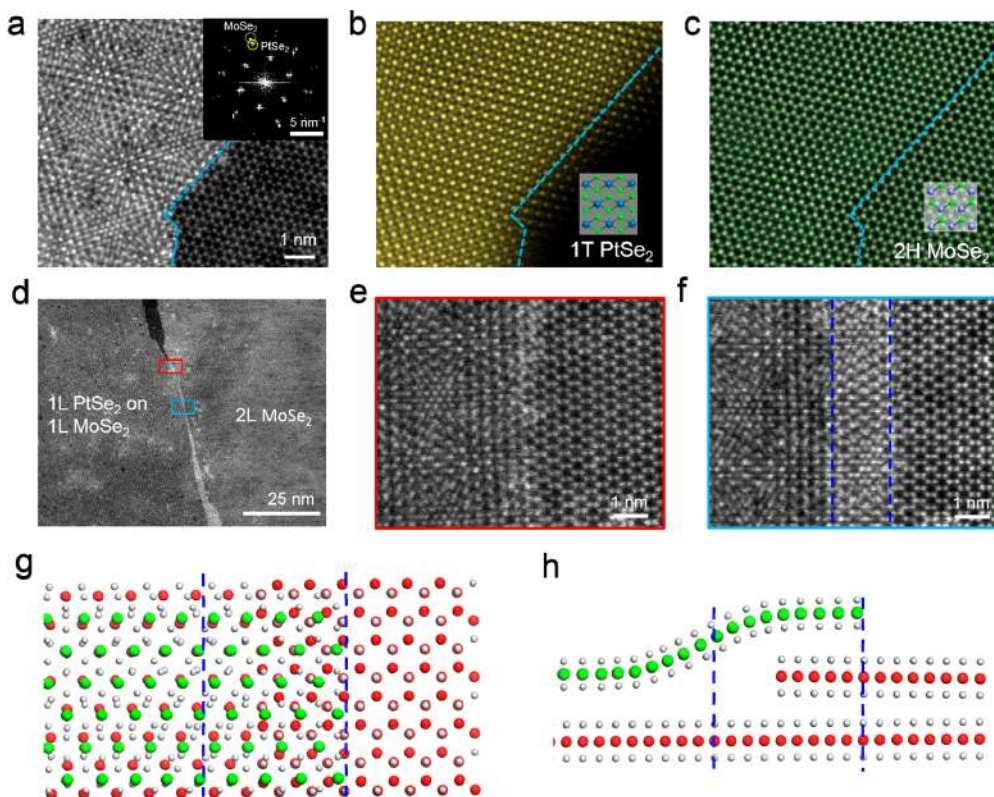


Figure 2. Atomic structure of the vertically stacked PtSe₂/MoSe₂ heterostructure and lateral boundary. (a) Experimental atomic-resolution ADF-STEM image of PtSe₂/MoSe₂, showing the periodic Moiré pattern where the monolayer PtSe₂ stacks on top of monolayer MoSe₂. Inset shows the FFT pattern obtained from (a), where the lattice constants of 0.376 and 0.332 nm correspond to the lattice of PtSe₂ and MoSe₂, as highlighted by the yellow and green circles, respectively. (b and c) Inverse FFT image of (a) by selectively filtering out the PtSe₂ (b) and MoSe₂ (c) lattice information in the FFT pattern, respectively. The 1T phase of PtSe₂ and 1H phase of MoSe₂ are confirmed by their discrete contrast which are consistent with the overlaid atomic models. (d) Low-magnification STEM image of the lateral boundary in a bilayer region. The left part is the PtSe₂/MoSe₂ heterostructure, while the right part is bilayer MoSe₂. (e and f) Atomic-resolution images of the highlighted regions in (d), showing the initial stage (e) and the overlapping region (f) of the lateral boundary. The initial stage shows a sharp change from PtSe₂ to MoSe₂ lattice with some tiny regions of bright contrast along the edge, indicating both PtSe₂ and MoSe₂ lattices have a sharp edge termination without any chemical bonding. The PtSe₂ and MoSe₂ gradually overlapped with each other along the boundary. (g and h) The top (g) and side (h) views of the schematic atomic models of the overlapping lateral boundary.

84 demonstrates its potential in electronic and optoelectronic
85 devices.

86 RESULTS AND DISCUSSION

87 Herein, the epitaxial growth of PtSe₂ on MoSe₂ was achieved
88 by using PtCl₂ and MoO₃/NaCl mixed powders as sources.¹⁴
89 More information about the growth is provided in the
90 Methods section. Figure 1a illustrates the reaction system for
91 the growth of PtSe₂ crystals. Figure 1b shows the proposed
92 growing mechanism. Monolayer PtSe₂ single crystals were
93 obtained on a MoSe₂ substrate with a one-step CVD method,
94 as shown in Figure 1c,d. Generally, most of the as-grown
95 samples were vertically stacked PtSe₂/MoSe₂. We believe that
96 the large lattice mismatch between PtSe₂ and MoSe₂ (1T for
97 PtSe₂ and 1H for MoSe₂) hinders the epitaxial growth of PtSe₂
98 and MoSe₂ in-plane heterostructure. Figure 1c shows the
99 hexagonal PtSe₂ monolayers atop the MoSe₂ monolayer with a
100 lateral size of ~30 μm. Such size is much larger than the
101 previously reported value.¹³ Atomic force microscopy (AFM)
102 was conducted to determine the height of the as-prepared
103 PtSe₂/MoSe₂ heterostructure. The thickness of PtSe₂ is ~0.8
104 nm, confirming its monolayer nature (Figure S1). More optical
105 images along with the size distribution of PtSe₂ flakes are
106 provided in Figure S2. The second layer MoSe₂ which coexists

with monolayer PtSe₂ can also be found in some synthesized 107
samples. The area of the PtSe₂/MoSe₂ heterostructure (Figure 108
1c) can be up to ~1000 μm². The size comparison is shown in 109
Figure S3.^{15–22} Meanwhile, we also observed that PtSe₂ 110
monolayers can grow not only epitaxially on top of MoSe₂ 111
but also partially overlap with MoSe₂ due to the different 112
growing rates of PtSe₂ and MoSe₂, as shown in Figure 1d. This 113
should be attributed to the nucleation formation of PtSe₂ on 114
the edge of MoSe₂, which then grows outward (down the 115
step). The Raman spectrum and thickness of PtSe₂ with a 116
similar morphology is shown in Figure S4. 117

In order to demonstrate the role of MoSe₂, time-dependent 118
experiments were carried out. For a short growing time (3 119
min), only MoSe₂ can be observed. By increasing the growing 120
time to 10 min, the PtSe₂/MoSe₂ heterostructure can be 121
obtained (see Figure S5). We also used different substrates 122
including exfoliated MoSe₂ flakes, SiO₂/Si, and sapphire wafers 123
to synthesize PtSe₂ crystals. Only PtSe₂ thick flakes and 124
particles can be obtained on exfoliated MoSe₂ flakes (Figure 125
S6). For SiO₂/Si and sapphire substrates, at the growing 126
temperature of ~400 °C, only polycrystalline PtSe₂ films can 127
be obtained (Figure S7). Increasing the growing temperature 128
to ~810 °C will result in few-layer PtSe₂ single crystal (Figures 129
S8 and S9). These results are consistent with previous reports 130

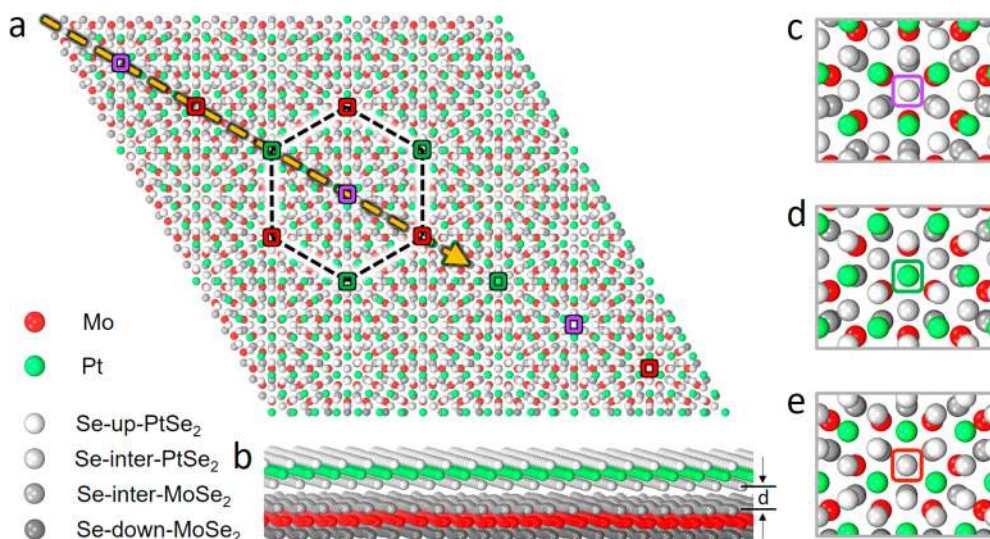


Figure 3. Geometry information on PtSe₂(1T)/MoSe₂(1H) vertical heterostructures. (a and b) Top and side views of the geometry structure of PtSe₂(1T)/MoSe₂(1H) vertical heterostructures. The violet, green, and red rectangles denote three high-symmetry stacking local configurations which have been zoomed in (c) Se_{inter}(PtSe₂)–Se_{inter}(MoSe₂) stacking, (d) Pt–Se_{inter}(MoSe₂) stacking, and (e) Se_{inter}(PtSe₂)–Mo stacking, respectively. And parameter *d* marked in (b) refers to the interlayer distance between PtSe₂(1T) and MoSe₂(1H).

131 on the growth of PtSe₂ flakes on MoSe₂.^{9,13} Based on these
132 results, it can be concluded that the CVD-grown MoSe₂
133 monolayer is a good candidate for the epitaxial growth of
134 PtSe₂ monolayer.

135 The successful growth of PtSe₂ monolayer on MoSe₂ can be
136 attributed to the following two reasons: (1) The chemical
137 reactivity between Mo precursors and Se is higher than that
138 between Pt precursor and Se and the vapor pressure of Mo
139 precursors is relatively higher than that of Pt precursor.¹⁴ As a
140 result, the growing rate of MoSe₂ is faster than that of PtSe₂,
141 which makes MoSe₂ grow first. (2) The lattice mismatch
142 between PtSe₂ and MoSe₂ is smaller than that between PtSe₂
143 and SiO₂/Si (or Al₂O₃). Therefore, MoSe₂ is a favorable
144 substrate for the epitaxial growth of PtSe₂ monolayer
145 (comparison is provided in Table S1). We also noticed that,
146 at a relatively high growing temperature (~810 °C), MoSe₂
147 flakes could be etched by H₂, which will result in MoSe₂ flakes
148 with different geometries.

149 Raman spectroscopy was carried out to investigate the
150 structure and quality of formed PtSe₂/MoSe₂ heterostructures.
151 Figure 1e shows the Raman spectra collected from points 1
152 and 2 of the sample shown in Figure 1c. The sole peak located
153 at 240 cm⁻¹ from point 1 (blue curve) corresponds to the A_{1g}
154 mode of MoSe₂.²³ Raman peaks sitting at 175, 205, and 240
155 cm⁻¹ were collected from point 2 (red curve), corresponding
156 to the E_g and A_{1g} modes of PtSe₂²⁴ and the A_{1g} mode of
157 MoSe₂, respectively. Notably, the A_{1g} mode of MoSe₂ in the
158 PtSe₂/MoSe₂ heterostructure shows a red shift due to the
159 interlayer coupling between PtSe₂ and MoSe₂, which is
160 consistent with the experimental observations reported result¹¹
161 and theoretical results.²⁵ Interestingly, from point 2, a Raman
162 peak located at ~350 cm⁻¹ can be found, which could be
163 attributed to the interlayer coupling between PtSe₂ and
164 MoSe₂.²⁶ These results confirm the vertically stacked PtSe₂/
165 MoSe₂ heterojunction. Next, we employed X-ray photo-
166 electron spectroscopy (XPS) to examine the composition of
167 the PtSe₂/MoSe₂ heterostructures. Based on XPS data (Figure
168 S10), the atomic ratio between Se and Pt/Mo is estimated to

be ~1.97, which is very close to the stoichiometry of MoSe₂
and PtSe₂. More information about the PL spectra and PL and
Raman mappings of PtSe₂/MoSe₂ heterostructures is pre-
sented in Figure S11. Note that the weak PL intensity of
PtSe₂/MoSe₂ heterostructures probably results from the charge
transfer between PtSe₂ and MoSe₂.

ADF-STEM was used to investigate the atomic structure of
PtSe₂/MoSe₂ heterostructures. Figure 2a shows the atomic-
resolution ADF-STEM image of PtSe₂/MoSe₂. The periodic
Moiré patterns can be clearly observed along the basal plane of
the heterostructure, which is caused by the interference from
the lattice of monolayer PtSe₂ and MoSe₂. The fast Fourier
transformation (FFT) of the PtSe₂/MoSe₂ is shown in the
inset of Figure 2a. Two different sets of diffraction patterns
close to each other were identified. The lattice constants of
~0.38 nm and ~0.33 nm correspond to PtSe₂ and MoSe₂
respective lattices, indicating the as-synthesized PtSe₂ and
MoSe₂ are single crystals. This is further confirmed by the
selected area electron diffraction pattern collected on a much
larger region of PtSe₂/MoSe₂ (over ~5 μm in size), as shown
in Figure S12, which only displays one set of diffraction pattern
of PtSe₂ and MoSe₂, respectively. Moreover, the two
monolayer lattices are well aligned with each other, which is
a strong evidence of the vertically epitaxial growth. The FFT
(inset in Figure 2a) does not show the superlattice periodicity,
which is expected near the central bright spot, presumably due
to its weak signal. However, the periodicity of the Moiré
pattern can be directly measured in the atomically resolved
image by filtering out the lattice of PtSe₂ and MoSe₂ (see
Figure S13 for more details), which is estimated to be ~2.60
nm. Such a large supercell indicates the highly epitaxial feature
as a result of the coupling growth between the two materials.
Figure 2b,c shows the inverse FFT images of Figure 2a, which
distinguishes the atomic structures of the 1T and 1H phases in
PtSe₂ and MoSe₂, respectively.

Figure 2d shows a low magnification ADF-STEM image of
the lateral boundary in the PtSe₂/MoSe₂ heterostructure. The
optical image of a similar structure is shown in Figure S14. The

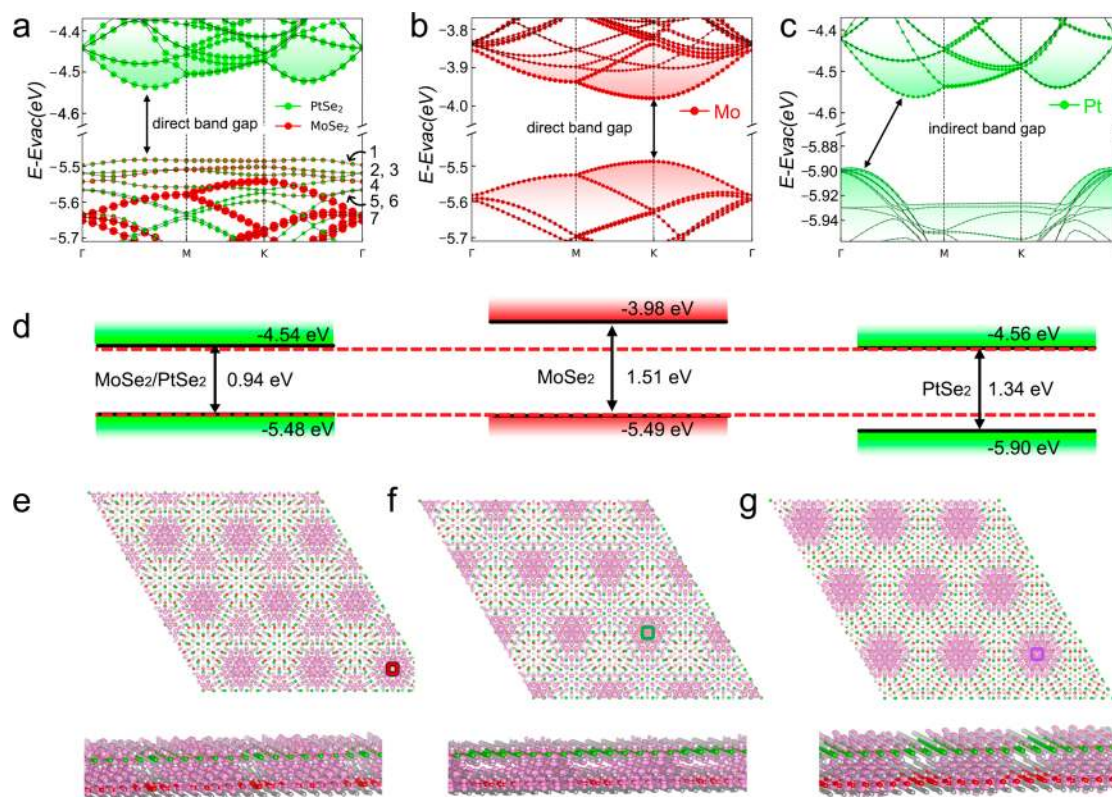


Figure 4. Band alignment and Spatial structures of wave functions for PtSe₂(1T)/MoSe₂(1H) vertical heterostructures. (a) The band structure of PtSe₂(1T)/MoSe₂(1H) vertical heterostructure as well as projected contributions of the marked systems. (b and c) Band structures and projected contributions of the marked atoms of deformed monolayer MoSe₂ and PtSe₂ whose geometry structures are extracted from the relaxed heterostructure. (d) Band alignment of original monolayer MoSe₂ and PtSe₂ and relaxed PtSe₂(1T)/MoSe₂(1H) vertical heterostructure. All energies here take the vacuum level as a reference. (e–g) Top and side views of the spatial distribution of modular squared wave functions for the marked bands 1, 4, and 7 in (a), separately. The violet, green, and red rectangles correspond to those in Figure 3. Side views display clearly each type of atom contribution to a certain band.

207 underneath MoSe₂ layer is continuous, thus such structure can
 208 be considered as a grain boundary between PtSe₂ and MoSe₂
 209 monolayers on the MoSe₂ substrate. Figure 2e,f shows
 210 atomically resolved images of two different regions along the
 211 lateral boundaries. In fact, because of the lattice mismatch
 212 between MoSe₂ and PtSe₂, the formation energy of an atomic
 213 sharp interface should be very high. Figure 2e shows the initial
 214 stage of the lateral boundary, displaying a sharp change from
 215 PtSe₂ to MoSe₂ lattice with some tiny regions of bright
 216 contrast along the edge. This indicates that both PtSe₂ and
 217 MoSe₂ lattices have a sharp edge termination without any
 218 chemical bonding. Figure 2f shows another region of the lateral
 219 boundary away from Figure 2e, where the transition region
 220 between the PtSe₂/MoSe₂ Moiré pattern and bilayer MoSe₂
 221 shows an enhanced contrast. This is due to the overlap of the
 222 edge regions from the two monolayers, that is, the PtSe₂ layer
 223 has rolled on top of the bilayer MoSe₂ edge, forming a thicker
 224 layer which exhibits brighter contrast, as illustrated by the
 225 corresponding atomic model (Figure 2g,h). The overlapping
 226 region varies and becomes wider (Figure 2d) along the
 227 boundary, confirming the overlapping feature in the lateral
 228 boundary. This is consistent with our expectation that the
 229 PtSe₂ is more likely to climb over the MoSe₂ edge (second
 230 layer MoSe₂) during the growth to form a vertically
 231 overlapping boundary since the formation energy of an
 232 interconnected in-plane boundary is very high, due to their
 233 lattice mismatch.

It is known that the interlayer interaction offers great
 opportunity to study different properties in van der Waals
 (vdW) solids, for instance, the electronic structure from the
 Moiré pattern in a vdW heterostructure.^{27–29} Substantial
 research efforts have been devoted to weak interlayer coupled
 TMDs and their heterostructures, for example, MoSe₂ and
 WSe₂.²⁷ Strong interlayer coupled two-dimensional (2D)
 materials have recently been visited,^{2,5,30,31} and PtSe₂ is a
 representative among them. An interesting question then arises
 regarding the interlayer coupling of a heterostructure whose
 components provide strong and weak interlayer couplings,
 respectively. The PtSe₂/MoSe₂ heterostructure synthesized
 in this work offers an ideal platform for studying this special
 interlayer interaction. The fully relaxed atomic structure of the
 PtSe₂(1T)/MoSe₂(1H) vertical heterostructure is shown in
 Figure 3. According to the STEM measured Moiré periodicity
 (Figure 2), a 7 × 7 supercell of the PtSe₂ monolayer stacking
 over an 8 × 8 supercell the MoSe₂ monolayer is adopted for
 modeling the heterostructure. The optimized lattice constant
 of the supercell is 2.64 nm, only 1.4% larger than the
 experimental value of 2.60 nm. It is exceptional that MoSe₂
 appears rumpling in the relaxed heterojunction, suggesting
 significant interlayer attraction (0.25 eV/PtSe₂) between the
 two layers and stronger bending strength of PtSe₂ than that of
 MoSe₂. The interlayer distance *d* varies from 3.15 to 3.64 Å,
 whose lower limit is much larger than that of PtSe₂ bilayers of
 2.55 Å⁵ but slightly smaller than that of MoSe₂ bilayers of 3.20
 Å,³² implying the interlayer interaction might be stronger than

262 that in MoSe₂. The mismatched lattices of 1L PtSe₂ (3.71 Å for
263 theory and 3.76 Å for experiment) and 1L MoSe₂ (3.30 Å for
264 theory and 3.32 Å for experiment) lead to continuously varied
265 stacking orders. There are seven local stacking orders along the
266 supercell lattice. Among them, we found three high-symmetry
267 ones, namely Se_{inter-PtSe₂} on top of Se_{inter-MoSe₂} (Figure 3c,
268 denoted by the violet rectangle), Pt on top of Se_{inter-MoSe₂}
269 (Figure 3d, denoted by the green rectangle), and Se_{inter-PtSe₂}
270 on top of Mo (Figure 3e, denoted by the red rectangle). The
271 vertical distances of these three stacking orders are 3.64, 3.17,
272 and 3.15 Å, respectively (Figure S15a). Correspondingly, the
273 spatial modulations of local bandgap and valence band
274 maximum (VBM) of this vertical heterostructure are shown
275 in Figures S15b, S16, and S17, respectively, where the
276 variations of bandgaps and VBMs share the same modulation
277 pattern with that of vertical interlayer distances. The Moiré
278 potential (VBM) for the above three high-symmetry stacking
279 orders are -6S, -5, and 0 meV, respectively.

280 Atom-decomposed band structures (Figure 4a) explicitly
281 show seven emerging states (denoted bands 1–7) in addition
282 to a type II band alignment of the heterojunctions. The valence
283 and conduction bands are comprised of the VB of MoSe₂ (Mo-
284 d orbital, Se-p orbital) and CB of PtSe₂ (Pt-d orbital, Se-p
285 orbital), respectively (Figure 4b,c). Figure 4d illustrates the
286 band alignment before and after forming the heterojunction.
287 The junction has a direct bandgap of 0.94 eV (0.92 eV, w/
288 SOC), reduced from a 1.51 eV (1.39 eV, w/SOC) direct
289 bandgap of MoSe₂ and a 1.34 eV (1.19 eV, w/SOC) indirect
290 bandgap of PtSe₂, which are in good accordance with their
291 experimental values, that is, 1.55 eV for MoSe₂³³ and 1.13 eV
292 for PtSe₂.⁵ These seven bands are not induced by the
293 aforementioned substantial structural deformation of MoSe₂
294 or PtSe₂, as Figure 4b,c shows that the deformation does not
295 change the shape of band structures. They are also not the case
296 of quantum confined states²⁹ since both MoSe₂ and PtSe₂
297 contribute to them. Bands 1–7 are thus regarded as
298 electronically hybridized interfacial states, which result from
299 the frustrated strong-weak interlayer coupling between PtSe₂
300 and MoSe₂ layers. These hybridized interfacial states, emerging
301 within the original bandgap of vdW heterojunctions, are of
302 particular interest. Figure 4e–g plots the spatial distributions of
303 the wave function norms of bands 1 (e), 4 (f) and 7 (g). They
304 are located around the aforementioned three particular
305 stacking positions as marked by red, green, and violet
306 rectangles, respectively, indicating each interfacial state
307 corresponds to one stacking configuration. The side views
308 (Figure 4e–g) suggest that these interfacial states are
309 comprised of p_z orbitals of the interfacial Se layer of MoSe₂
310 and both Se layers of PtSe₂ and d_{z²} orbital of Pt and Mo atoms,
311 implying that the outer Se layer of MoSe₂ is not involved in
312 forming these interfacial states. These wave functions are more
313 localized than those of VB and CB (Figure S18) in real-space,
314 consistent with the flat band dispersion in the *k*-space. These
315 spatially localized bands suggest that electron–hole pairs of a
316 given energy are excited at a certain stacking position, as
317 marked in Figure 3a. The PtSe₂ involved in forming these
318 bands may lead to inter- and intralayer mixed excitation
319 mechanisms for the interlayer excitons, which should be
320 interesting for further exploration. In the light of these,
321 interfacial states are of particular interest in terms of exciton
322 dynamics in the heterojunction.

As discussed above, STEM images and first-principles
calculations have demonstrated the vertical stacking and
emerging interfacial states in PtSe₂/MoSe₂ heterostructure
due to the frustrated strong–weak interlayer coupling between
PtSe₂ and MoSe₂ layers. In order to further elucidate the
interfacial states and the interlayer coupling, we conducted the
electrostatic force microscopy (EFM) to study the charge
distribution in PtSe₂/MoSe₂ heterostructures. EFM has been
proven as an effective method to evaluate the local electrical
properties of 2D materials.^{34,35} The optical image and
topography of PtSe₂/MoSe₂ heterostructure are shown in
Figure 5a,c, respectively. The corresponding AFM image is

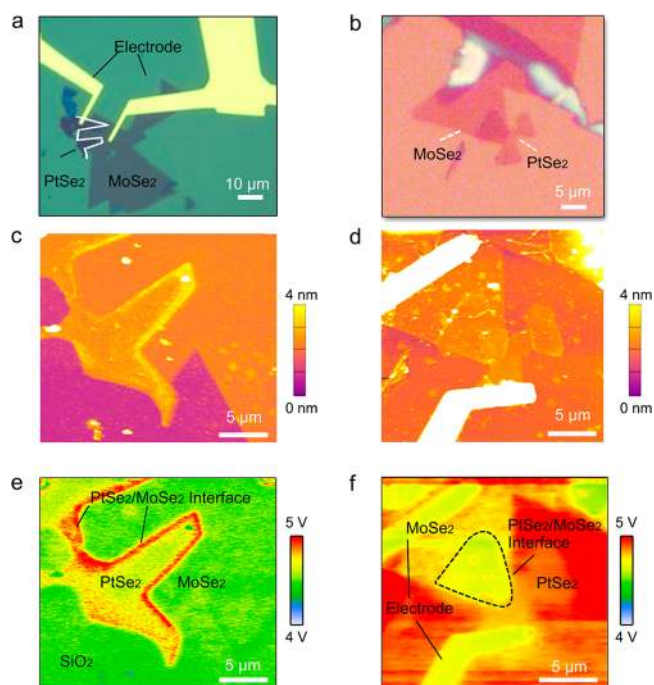


Figure 5. EFM measurements. (a and c) Optical image and height topography of PtSe₂/MoSe₂ heterostructure grown by one-step CVD. (b and d) Optical image and topography of transferred PtSe₂/MoSe₂ heterostructure. (e) EFM image of PtSe₂/MoSe₂, identifying the edge state at the edge of PtSe₂. (f) EFM image of transferred PtSe₂/MoSe₂ under zero bias voltage, indicating a semiconducting behavior of PtSe₂ and MoSe₂.

presented in Figure S19. The EFM image of the hetero-
structure shown in Figure 5e indicates that strong charge
accumulation takes place on the edge of PtSe₂, which is
attributed to the charge transfer from uncovered monolayer
MoSe₂ to PtSe₂/MoSe₂ heterostructure induced by the slightly
lowered VB of PtSe₂ and lifted CB of MoSe₂. For comparison,
EFM measurement was carried out on a transferred PtSe₂/
MoSe₂ heterostructure. The optical image, topography, and
EFM image are shown in Figure 5b,d,f, respectively. The
absence of edge states clearly illustrates that the strong
interlayer coupling is not formed in the transferred
heterostructure. These results demonstrate the strong inter-
layer coupling between strong interlayer-coupled PtSe₂ and
weak interlayer-coupled MoSe₂, which agrees well with the
results of electronically hybridized interface states from first-
principles calculations.

The type II band alignment offers the possibility to study the
charge transfer induced by the interlayer coupling in PtSe₂/
MoSe₂.

MoSe₂ heterostructure. We further studied the charge transfer kinetics of PtSe₂/MoSe₂ heterostructure through ultrafast transient dynamics measurement. The ultrafast transient reflection dynamics of the heterostructure along with the PtSe₂ and MoSe₂ monolayers (optical images are shown as insets in Figure 6a,b) were measured using 910 nm pump

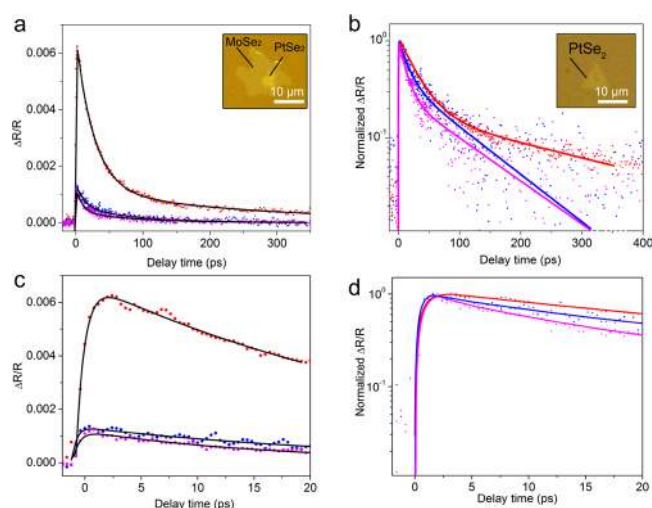


Figure 6. Ultrafast electron dynamics of MoSe₂, PtSe₂, and PtSe₂/MoSe₂ heterostructure. (a) Differential reflection kinetics of PtSe₂/MoSe₂ heterostructure (red), PtSe₂ (blue), and MoSe₂ (pink) monolayers excited at 910 nm and probed at 780 nm with the pump and probe power around 100 and 70 μW, respectively. Inset is the optical image of PtSe₂/MoSe₂ heterostructure. The kinetics at shorter time scale is shown in (c). (b) Comparison of the normalized differential reflection kinetics of the heterostructure and monolayers. Inset is the optical image of PtSe₂. The corresponding kinetics at shorter time scale of PtSe₂ is displayed in (d).

excitation and 780 nm probe with pump and probe powers of 100 and 70 μW, respectively. According to the reported experimental band gaps of monolayer MoSe₂ (1.55 eV)³³ and PtSe₂ (1.13 eV)⁵ as well as our band calculation results, the 910 nm pump excitation will only excite carriers in PtSe₂, since the photon energy is below the bandgap of MoSe₂. Thus, direct one-photon absorption of 910 nm wavelength will not occur in MoSe₂ layers. As shown in Figure 6, the transient response from the heterostructure is very different from that of monolayers under the same pump–probe power. First, the transient response amplitude of the heterostructure is ~3 times higher than that of individual monolayers (Figure 6a). Second, the initial rising time of the transient response is slightly slower in heterostructure than that in individual monolayers. Third, the subsequent decay dynamics are relatively longer for heterostructure than either PtSe₂ or MoSe₂ monolayer alone. The latter two features can be clearly visualized from the normalized transient reflection kinetics shown in Figure 6b.

Compared with monolayer PtSe₂, the relatively slow rising kinetics of the PtSe₂/MoSe₂ heterostructure proves the hole transfer between PtSe₂ and MoSe₂. More specifically, the pump (910 nm) excites electrons from the VB to the CB of PtSe₂ through one photon absorption, along with a rapid hole transfer from PtSe₂ to MoSe₂ layer due to their type II band alignment. The rising time (τ_r) of the heterostructure kinetics, which describes the hole transfer between PtSe₂ and MoSe₂, is found to be 0.5–0.9 ps. This value is longer than that of PtSe₂

monolayers and consistent with the previous reports on the charge-transfer process in heterostructures.³⁶ As a result of the hole transfer from PtSe₂ to MoSe₂, the probe reflection is modified due to the hole occupation in MoSe₂ and contributes to transient reflection signal of the 780 nm probe. The magnitude of peak transient signal is also 5 times larger than that in individual PtSe₂ or MoSe₂ monolayers.

The following decay kinetics after the maximum transient reflection of the heterostructure and monolayers can be fitted with biexponential function $I(t) = A \times \exp(-t/\tau_{d1}) + B \times \exp(-t/\tau_{d2})$, where τ_{d1} and τ_{d2} represent the fast and slow decay time constants, respectively. The fast ($\tau_{d1} = 27.5 \pm 0.3$ ps) and slow ($\tau_{d2} = 280.1 \pm 12.3$ ps) decay time constants of the heterostructure are nearly 2–3 times larger than decay time constants of individual PtSe₂ ($\tau_{d1} = 14.9 \pm 1.8$ ps, $\tau_{d2} = 88.8 \pm 9$ ps) and MoSe₂ ($\tau_{d1} = 11.7 \pm 0.9$ ps, $\tau_{d2} = 97.9 \pm 9$ ps) monolayers. The decay time of PtSe₂/MoSe₂ heterostructure is much longer than that of PtSe₂ and MoSe₂ monolayers, which suggests an efficient separation of the electron–hole in PtSe₂/MoSe₂ heterostructures.

CONCLUSIONS

In summary, we have successfully synthesized PtSe₂/MoSe₂ vertically stacked heterojunctions *via* a one-step CVD method. STEM results confirm the formation of vertical and lateral heterostructures between strong interlayer-coupled PtSe₂ and weak interlayer-coupled MoSe₂. First-principle calculations confirm a direct band gap structure and type II band alignment between PtSe₂ and MoSe₂. The emerging electronically hybridized interface states within the original bandgap are the observed in CVD-grown 2D TMD heterostructures, which have been confirmed by the edge states unveiled by EFM. Ultrafast electron dynamics measurements suggest that the holes transfer from MoSe₂ to PtSe₂, confirming the theoretically predicted band alignment and strong interlayer coupling between PtSe₂ and MoSe₂. This strategy shows the way toward the synthesis of heterostructures based on group 10 TMDs, and our results show great potential of PtSe₂/MoSe₂ heterostructures for applications in electronic and optoelectronic devices.

METHODS

PtSe₂ and PtSe₂/MoSe₂ Growth. In our experiment, PtCl₂, MoO₃, and Se were used as sources (all reactants were bought from Alfa Aesar with purity more than 99%). The polycrystalline PtSe₂ film was grown in a quartz tube (1 in. diameter, 36 cm length) at 400 °C. Single PtSe₂ and PtSe₂/MoSe₂ flakes were synthesized using the same setup at 810 °C. The distance between PtCl₂ and mixed powder is ~5 mm. H₂/Ar was used as the carrier gas. Specifically, the alumina boat (8 cm × 1.1 cm × 1.2 cm) containing Mo and Pt precursors was put in the middle of the quartz tube. The distance between the precursors and substrate is around 1.2 cm. For PtSe₂, Ar (or Ar/H₂ mix) gas with a flow rate of 80 (80/10) sccm was used as the carrier gas, and the Al₂O₃ boat containing 10 mg PtCl₂ was put in the center of the tube. The SiO₂/Si substrate was placed on the boat with surface downside. Another Al₂O₃ boat containing 100 mg Se powder was put in the upstream zone. The temperature was ramped up to 810 °C in 16 min and kept at the reaction temperature for 15 min. Then the furnace was cooled down to room temperature naturally.

For PtSe₂/MoSe₂, the Ar/H₂ mixed gas with a flow rate of 80/10 sccm was used as the carrier gas, and the Al₂O₃ boat containing 5 mg PtCl₂ and 5 mg (4 mg MoO₃ and 1 mg NaCl) was put in the center of the tube. The distance between PtCl₂ and MoO₃/NaCl was 5 mm. SiO₂/Si or sapphire substrate was placed on the boat with surface downside. Another Al₂O₃ boat containing 10 g Se powder was put on

449 the upstream zone. The temperature was ramped up to 810 °C in 16
450 min and kept at the reaction temperature for 10 min. The furnace was
451 then cooled down to room temperature gradually.

452 For PtSe₂/MoSe₂ heterostructure prepared by mechanic exfoliation
453 and transfer, a 0.8 μm layer of poly(methyl methacrylate) (PMMA)
454 was spin-coated on the MoSe₂ wafer and then baked at 180 °C for 4
455 min. Afterward, the wafer was immersed in KOH solution (1M) to
456 etch the SiO₂ layer. After lift-off, the PMMA/PtSe₂/MoSe₂ film was
457 transferred into DI water for several cycles to wash away the residual
458 contaminants and then dried in air. Next, PMMA with MoSe₂ samples
459 were transferred on PtSe₂ flakes. Last, the wafer was immersed in
460 acetone solution to resolve the PMMA.

461 **Raman Characterization.** Raman measurements with an
462 excitation laser of 532 nm were performed using WITEC alpha
463 300R Confocal Raman system. Before Raman characterization, the
464 system was calibrated with the Raman peak of Si at 520 cm⁻¹. The
465 laser powers were set at <1 mW to avoid overheat the samples.

466 **AFM.** AFM measurement was carried out using the Asylum
467 Research, Cypher S system with a cantilever tip of Arrow-NCR-50-
468 Silicon SPM-Sensor (coating on detector sider: Al-coating). The force
469 constant is 42 N/m.

470 **XPS Characterization.** XPS measurement was performed using a
471 monochromated Al Kα source ($h\nu = 1486.6$ eV) and a 128 channel
472 mode detection PHI original detector. XPS spectra were acquired at a
473 pass energy of 140 eV and takeoff angle of 45°.

474 **TEM and STEM Characterization.** The STEM samples were
475 prepared with a PMMA assisted method. A layer of PMMA about 0.8
476 μm in thickness was spin-coated on the wafer with samples deposited
477 and then baked at 140 °C for 5 min. Afterward, the wafer was
478 immersed in KOH solution (1 M) to etch the SiO₂ layer overnight.
479 After lift-off, the PMMA/PtSe₂/MoSe₂ film was transferred into DI
480 water for several cycles to wash away the residual contaminants and
481 then fished by a TEM grid (Quantifoil Mo grid). The transferred
482 specimen was dried naturally in ambient environment and then
483 dropped into acetone overnight to wash away the PMMA coating
484 layers. The STEM imaging was done in a JEOL 2100F with delta
485 probe corrector, which corrects the aberration up to fifth order,
486 resulting in a probe size of 1.2 Å. The imaging was conducted at an
487 acceleration voltage of 60 kV. The convergent angle for illumination is
488 about 35 mrad, with a collection detector angle ranging from 45 to
489 200 mrad. The BF-TEM and diffraction imaging was conducted in a
490 FEI Tecnai F30 microscope operating at 80 kV. All imaging was
491 performed at room temperature.

492 **Ultrafast Transient Reflection Spectroscopy.** An infrared
493 optical parametric amplifier (OPA) pumped by a 60 fs, 250 kHz
494 Ti:Sapphire regenerative amplifier (RegA) was used in the transient
495 reflection measurements. The idler from OPA at 1840 nm used as
496 pump is frequency doubled to 920 nm (~180 fs). The 780 nm
497 component filtered from white light supercontinuum, which is
498 generated from a sapphire crystal pumped with compressed remnant
499 800 nm beam of OPA, was used as a probe. Both pump and probe
500 pulses were linearly polarized. A 40× reflective objective lens was used
501 to focus the co-propagating pump probe spots onto the sample. The
502 reflected probe was collected by the same objective lens and routed
503 through a monochromator followed by a photodetector. The detected
504 probe reflection was read by a lock-in amplifier referenced to a
505 mechanically chopped pump. The probe spot size was estimated to be
506 2 μm. The pump photon fluency was estimated to be around 1×10^{16}
507 photons/cm².

508 **Calculations.** Density functional theory (DFT) calculations were
509 performed using the generalized gradient approximation for the
510 exchange–correlation potential, the projector augmented wave
511 method,^{37,38} and a plane-wave basis set as implemented in the
512 Vienna *ab initio* simulation package (VASP).³⁹ For the configuration
513 of PtSe₂(1T)/MoSe₂(1H) vertical heterostructure, a (7 × 7) supercell
514 is adopted for PtSe₂(1T), while a (8 × 8) supercell for MoSe₂(1H)
515 and a vacuum layer of 25 Å in thickness between periodic images was
516 employed. The energy cutoff for the plane-wave basis was set to 500
517 eV for all calculations except those with spin–orbit coupling (SOC)
518 into consideration where an energy cutoff of 300 eV is utilized. The

inclusion of SOC has little influence on the shape of the band 519
structures but induces appreciable band energy shifts or band 520
splitting, for example, a separation of 30–50 meV for the emerging 521
hybridized interfacial states marked with bands 1–7 in Figure 4a. All 522
calculations and analysis shown in Figure 4a–c were performed in the 523
same supercell which consisted of a (7 × 7) supercell of PtSe₂(1T) 524
and a (8 × 8) supercell of MoSe₂(1H). In optimizing the system 525
geometry, vdW interactions were considered at the vdW-DF⁴⁰ level 526
with the optB86b (optB86b-vdW) functional for exchange potential,⁴¹ 527
which was recently demonstrated more accurate in describing 528
structural properties of layered materials than other functionals.^{31,42,43} 529
All atoms in the supercell were allowed to relax until the residual force 530
per atom was <0.02 eV·Å⁻¹. 531

ASSOCIATED CONTENT

Supporting Information

The Supporting Information is available free of charge on the 534
ACS Publications website at DOI: 10.1021/acsnano.8b09479. 535

Further experimental and theoretical details, including 536
different size of vertical heterostructures, thickness and 537
Raman spectrum of PtSe₂, optical images of PtSe₂/ 538
MoSe₂ heterostructure, growth of PtSe₂ on exfoliated 539
MoSe₂ flakes, optical image and TEM characterization of 540
polycrystalline PtSe₂, optical images, AFM images and 541
Raman spectra of PtSe₂ single crystals, optical images 542
and AFM images of PtSe₂ single crystals synthesized on 543
sapphire substrate, XPS characterizations of PtSe₂/ 544
MoSe₂ heterostructure, PL spectra, PL and Raman 545
mappings of PtSe₂/MoSe₂ with different shape, SEAD 546
patterns of PtSe₂/MoSe₂ heterostructure, large-scale 547
STEM image of vertically stacked PtSe₂/MoSe₂ 548
heterostructure, optical image of in plane and vertical 549
PtSe₂/MoSe₂ heterostructures, spatial distribution of 550
interlayer distance and bandgap for PtSe₂(1T)/ 551
MoSe₂(1H) vertical heterostructure, spatial distribution 552
of bandgap for PtSe₂(1T)/MoSe₂(1H) vertical hetero- 553
structure, spatial distribution of VBM for PtSe₂(1T)/ 554
MoSe₂(1H) vertical heterostructure, spatial structures of 555
wave functions for PtSe₂(1T)/MoSe₂(1H) vertical 556
heterostructures, AFM image and thickness of PtSe₂ 557
on MoSe₂ (PDF) 558

AUTHOR INFORMATION

Corresponding Authors

*E-mail: z.liu@ntu.edu.sg. 560

*E-mail: wji@ruc.edu.cn. 561

*E-mail: sundong@pku.edu.cn. 562

*E-mail: lin.junhao.stem@gmail.com. 563

ORCID

Xianghua Kong: 0000-0003-4381-4955 565

Zhihai Cheng: 0000-0003-4938-4490 566

Ting Yu: 0000-0001-5782-1588 567

Kazu Suenaga: 0000-0002-6107-1123 568

Dong Sun: 0000-0002-0898-4548 569

Wei Ji: 0000-0001-5249-6624 570

Zheng Liu: 0000-0002-8825-7198 571

Author Contributions

•These authors contributed equally to this work. 572

Notes

The authors declare no competing financial interest. 573

577 ACKNOWLEDGMENTS

578 This work is supported by the Singapore National Research
579 Foundation under NRF RF award no. NRF-RF2013-08. MOE
580 Tier 1 RG7/18, MOE Tier 2 MOE2015-T2-2-007, MOE2016-
581 T2-2-153, MOE2017-T2-2-136, MOE Tier 3 MOE2018-T3-1-
582 002, and A*Star QTE program. J.L. and K.S. acknowledge JST-
583 ACCEL and JSPS KAKENHI (JP16H06333 and P16823) for
584 financial support. This work was also supported by the Pico
585 Center at MCPC of SUSTech that receives support from
586 Presidential fund and Development and Reform Commission
587 of Shenzhen Municipality. Z.-H.L. thanks the A*STAR Science
588 and Engineering Research Council (122 360 0008) and the
589 Ministry of Education (MOE2014-T2-2-052) for financial
590 support. Z.H.C. thanks the Ministry of Science and
591 Technology (MOST) of China (no. 2016YFA0200700) for
592 financial support. X.K. Z.H.C., R.X., and W.J. were supported
593 by the National Natural Science Foundation of China (grant
594 nos. 11274380, 91433103, 11622437, 21622304, 61674045,
595 11604063, and 61674171), the Fundamental Research Funds
596 for the Central Universities of China and the Research Funds
597 of Renmin University of China (grant nos. 16XNLQ01 and
598 18XNLG01), and the Strategic Priority Research Program of
599 Chinese Academy of Sciences (grant no. XDB30000000). This
600 research is partially supported by the Science, Technology, and
601 Innovation Commission of Shenzhen Municipality (no.
602 ZDSYS20170303165926217). X.K. thanks Prof. Hong Guo
603 at McGill University for financial support. C.M., W.L., and D.S.
604 were supported by the National Natural Science Foundation of
605 China (grant nos. 11674013, 11704012). Calculations were
606 performed at the physics lab of high-performance computing of
607 Renmin University of China, Shanghai Supercomputer Center,
608 McGill University, Calcul Québec, and Compute Canada.

609 REFERENCES

610 (1) Yao, W.; Wang, E. Y.; Huang, H. Q.; Deng, K.; Yan, M. Z.;
611 Zhang, K. N.; Miyamoto, K.; Okuda, T.; Li, L. F.; Wang, Y. L.; Gao,
612 H. J.; Liu, C. X.; Duan, W. H.; Zhou, S. Y. Direct Observation of Spin-
613 Layer Locking by Local Rashba Effect in Monolayer Semiconducting
614 PtSe₂ Film. *Nat. Commun.* **2017**, *8*, 142216.
615 (2) Zhao, Y. D.; Qiao, J. S.; Yu, P.; Hu, Z. X.; Lin, Z. Y.; Lau, S. P.;
616 Liu, Z.; Ji, W.; Chai, Y. Extraordinarily Strong Interlayer Interaction in
617 2D Layered PtS₂. *Adv. Mater.* **2016**, *28*, 2399–2407.
618 (3) Ciarrocchi, A.; Avsar, A.; Ovchinnikov, D.; Kis, A. Thickness-
619 Modulated Metal-to-Semiconductor Transformation in a Transition
620 Metal Dichalcogenide. *Nat. Commun.* **2018**, *9*, 919.
621 (4) Li, P. F.; Li, L.; Zeng, X. C. Tuning the Electronic Properties of
622 Monolayer and Bilayer PtSe₂ via Strain Engineering. *J. Mater. Chem. C*
623 **2016**, *4*, 3106–3112.
624 (5) Zhao, Y. D.; Qiao, J. S.; Yu, Z. H.; Yu, P.; Xu, K.; Lau, S. P.;
625 Zhou, W.; Liu, Z.; Wang, X. R.; Ji, W.; Chai, Y. High-Electron-
626 Mobility and Air-Stable 2D Layered PtSe₂ FETs. *Adv. Mater.* **2017**,
627 *29*, 1604230.
628 (6) Zeng, L.; Lin, S.; Lou, Z.; Yuan, H.; Long, H.; Li, Y.; Lu, W.;
629 Lau, S. P.; Wu, D.; Tsang, Y. H. Ultrafast and Sensitive Photodetector
630 Based on a PtSe₂/Silicon Nanowire Array Heterojunction with a
631 Multiband Spectral Response from 200 to 1550 nm. *NPG Asia Mater.*
632 **2018**, *10*, 352–362.
633 (7) Yu, X. C.; Yu, P.; Wu, D.; Singh, B.; Zeng, Q. S.; Lin, H.; Zhou,
634 W.; Lin, J. H.; Suenaga, K.; Liu, Z.; Wang, Q. J. Atomically Thin
635 Noble Metal Dichalcogenide: A Broadband Mid-Infrared Semi-
636 conductor. *Nat. Commun.* **2018**, *9*, 1545.
637 (8) Chia, X. Y.; Adriano, A.; Lazar, P.; Sofer, Z.; Luxa, J.; Pumera, M.
638 Layered Platinum Dichalcogenides (PtS₂, PtSe₂, and PtTe₂) Electro-
639 catalysis: Monotonic Dependence on the Chalcogen Size. *Adv. Funct.*
640 *Mater.* **2016**, *26*, 4306–4318.

(9) Yim, C.; Lee, K.; McEvoy, N.; O'Brien, M.; Riazimehr, S.;
641 Berner, N. C.; Cullen, C. P.; Kotakoski, J.; Meyer, J. C.; Lemme, M.
642 C.; Duesberg, G. S. High-Performance Hybrid Electronic Devices
643 from Layered PtSe₂ Films Grown at Low Temperature. *ACS Nano*
644 **2016**, *10*, 9550–9558.
645 (10) Liu, K.; Zheng, B. J.; Wu, J. J.; Chen, Y. F.; Wang, X. Q.; Qi, F.;
646 He, D. W.; Zhang, W. L.; Li, Y. R. Synthesis of Two-Dimensional
647 Semiconductor Single-Crystal PtSe₂ under High Pressure. *J. Mater.*
648 *Sci.* **2018**, *53*, 1256–1263.
649 (11) Yan, M. Z.; Wang, E. Y.; Zhou, X.; Zhang, G. Q.; Zhang, H. Y.;
650 Zhang, K. N.; Yao, W.; Lu, N. P.; Yang, S. Z.; Wu, S. L.; Yoshikawa,
651 T.; Miyamoto, K.; Okuda, T.; Wu, Y.; Yu, P.; Duan, W. H.; Zhou, S.
652 Y. High Quality Atomically Thin PtSe₂ Films Grown by Molecular
653 Beam Epitaxy. *2D Mater.* **2017**, *4*, 045015.
654 (12) Wang, Y. L.; Li, L. F.; Yao, W.; Song, S. R.; Sun, J. T.; Pan, J. B.;
655 Ren, X.; Li, C.; Okunishi, E.; Wang, Y. Q.; Wang, E. Y.; Shao, Y.;
656 Zhang, Y. Y.; Yang, H. T.; Schwier, E. F.; Iwasawa, H.; Shimada, K.;
657 Taniguchi, M.; Cheng, Z. H.; Zhou, S. Y.; et al. Monolayer PtSe₂, a
658 New Semiconducting Transition-Metal-Dichalcogenide, Epitaxially
659 Grown by Direct Selenization of Pt. *Nano Lett.* **2015**, *15*, 4013–4018.
660 (13) Wang, Z. G.; Li, Q.; Besenbacher, F.; Dong, M. D. Facile
661 Synthesis of Single Crystal PtSe₂ Nanosheets for Nanoscale
662 Electronics. *Adv. Mater.* **2016**, *28*, 10224–10229.
663 (14) Zhou, J. D.; Lin, J. H.; Huang, X. W.; Zhou, Y.; Chen, Y.; Xia,
664 J.; Wang, H.; Xie, Y.; Yu, H. M.; Lei, J. C.; Wu, D.; Liu, F. C.; Fu, Q.
665 D.; Zeng, Q. S.; Hsu, C. H.; Yang, C. L.; Lu, L.; Yu, T.; Shen, Z. X.;
666 Lin, H.; et al. A Library of Atomically Thin Metal Chalcogenides.
667 *Nature* **2018**, *556*, 355–359.
668 (15) Li, M. Y.; Shi, Y. M.; Cheng, C. C.; Lu, L. S.; Lin, Y. C.; Tang,
669 H. L.; Tsai, M. L.; Chu, C. W.; Wei, K. H.; He, J. H.; Chang, W. H.;
670 Suenaga, K.; Li, L. J. Epitaxial Growth of a Monolayer WSe₂-MoS₂
671 Lateral *p-n* Junction with an Atomically Sharp Interface. *Science* **2015**,
672 *349*, 524–528.
673 (16) Chen, K.; Wan, X.; Wen, J. X.; Xie, W. G.; Kang, Z. W.; Zeng,
674 X. L.; Chen, H. J.; Xu, J. B. Electronic Properties of MoS₂-WS₂
675 Heterostructures Synthesized with Two-Step Lateral Epitaxial
676 Strategy. *ACS Nano* **2015**, *9*, 9868–9876.
677 (17) Chen, K.; Wan, X.; Xie, W. G.; Wen, J. X.; Kang, Z. W.; Zeng,
678 X. L.; Chen, H. J.; Xu, J. B. Lateral Built-in Potential of Monolayer
679 MoS₂-WS₂ in-Plane Heterostructures by a Shortcut Growth Strategy.
680 *Adv. Mater.* **2015**, *27*, 6431–6437.
681 (18) Li, X. F.; Lin, M. W.; Lin, J. H.; Huang, B.; Puzos, A. A.; Ma,
682 C.; Wang, K.; Zhou, W.; Pantelides, S. T.; Chi, M. F.; Kravchenko, I.;
683 Fowlkes, J.; Rouleau, C. M.; Geoghegan, D. B.; Xiao, K. Two-
684 Dimensional GaSe/MoSe₂ Misfit Bilayer Heterojunctions by Van Der
685 Waals Epitaxy. *Sci. Adv.* **2016**, *2*, No. e1501882.
686 (19) Yoo, Y. D.; Degregorio, T. P.; Johns, J. E. Seed Crystal
687 Homogeneity Controls Lateral and Vertical Heteroepitaxy of
688 Monolayer MoS₂ and WS₂. *J. Am. Chem. Soc.* **2015**, *137*, 14281–
689 14287.
690 (20) Zhang, T.; Jiang, B.; Xu, Z.; Mendes, R. G.; Xiao, Y.; Chen, L.
691 F.; Fang, L. W.; Gemming, T.; Chen, S. L.; Rummeli, M. H.; Fu, L.
692 Twinned Growth Behaviour of Two-Dimensional Materials. *Nat.*
693 *Commun.* **2016**, *7*, 13911.
694 (21) Gong, Y. J.; Lin, J. H.; Wang, X. L.; Shi, G.; Lei, S. D.; Lin, Z.;
695 Zou, X. L.; Ye, G. L.; Vajtai, R.; Yakobson, B. I.; Terrones, H.;
696 Terrones, M.; Tay, B. K.; Lou, J.; Pantelides, S. T.; Liu, Z.; Zhou, W.;
697 Ajayan, P. M. Vertical and in-Plane Heterostructures from WS₂/MoS₂
698 Monolayers. *Nat. Mater.* **2014**, *13*, 1135–1142.
699 (22) Duan, X. D.; Wang, C.; Shaw, J. C.; Cheng, R.; Chen, Y.; Li, H.
700 L.; Wu, X. P.; Tang, Y.; Zhang, Q. L.; Pan, A. L.; Jiang, J. H.; Yu, R.
701 Q.; Huang, Y.; Duan, X. F. Lateral Epitaxial Growth of Two-
702 Dimensional Layered Semiconductor Heterojunctions. *Nat. Nano-*
703 *technol.* **2014**, *9*, 1024–1030.
704 (23) Wang, X. L.; Gong, Y. J.; Shi, G.; Chow, W. L.; Keyshar, K.; Ye,
705 G. L.; Vajtai, R.; Lou, J.; Liu, Z.; Ringe, E.; Tay, B. K.; Ajayan, P. M.
706 Chemical Vapor Deposition Growth of Crystalline Monolayer MoSe₂.
707 *ACS Nano* **2014**, *8*, 5125–5131.
708

- 709 (24) O'Brien, M.; McEvoy, N.; Motta, C.; Zheng, J. Y.; Berner, N.
710 C.; Kotakoski, J.; Elibol, K.; Pennycook, T. J.; Meyer, J. C.; Yim, C.;
711 Abid, M.; Hallam, T.; Donegan, J. F.; Sanvito, S.; Duesberg, G. S.
712 Raman Characterization of Platinum Diselenide Thin Films. *2D*
713 *Mater.* **2016**, *3*, 021004.
- 714 (25) Kim, K.; Lee, J. U.; Nam, D.; Cheong, H. Davydov Splitting
715 and Excitonic Resonance Effects in Raman Spectra of Few-Layer
716 MoSe₂. *ACS Nano* **2016**, *10*, 8113–20.
- 717 (26) Nam, D.; Lee, J. U.; Cheong, H. Excitation Energy Dependent
718 Raman Spectrum of MoSe₂. *Sci. Rep.* **2015**, *5*, 17113.
- 719 (27) Zhang, C. D.; Chuu, C. P.; Ren, X. B.; Li, M. Y.; Li, L. J.; Jin, C.
720 H.; Chou, M. Y.; Shih, C. K. Interlayer Couplings, Moire Patterns,
721 and 2D Electronic Superlattices in MoS₂/WSe₂ Hetero-Bilayers. *Sci.*
722 *Adv.* **2017**, *3*, No. e1601459.
- 723 (28) Hong, J. H.; Wang, C.; Liu, H. J.; Ren, X. B. A.; Chen, J. L.;
724 Wang, G. Y.; Jia, J. F.; Xie, M. H.; Jin, C. H.; Ji, W.; Yuan, J.; Zhang, Z.
725 Inversion Domain Boundary Induced Stacking and Bandstructure
726 Diversity in Bilayer MoSe₂. *Nano Lett.* **2017**, *17*, 6653–6660.
- 727 (29) Pan, Y.; Folsch, S.; Nie, Y. F.; Waters, D.; Lin, Y. C.; Jariwala,
728 B.; Zhang, K. H.; Cho, K.; Robinson, J. A.; Feenstra, R. M. Quantum-
729 Confined Electronic States Arising from the Moire Pattern of MoS₂-
730 WSe₂ Heterobilayers. *Nano Lett.* **2018**, *18*, 1849–1855.
- 731 (30) Qiao, J.; Pan, Y.; Yang, F.; Wang, C.; Chai, Y.; Ji, W. Few-Layer
732 Tellurium: One-Dimensional-Like Layered Elementary Semiconduc-
733 tor with Striking Physical Properties. *Sci. Bull.* **2018**, *63*, 159–168.
- 734 (31) Qiao, J. S.; Kong, X. H.; Hu, Z. X.; Yang, F.; Ji, W. High-
735 Mobility Transport Anisotropy and Linear Dichroism in Few-Layer
736 Black Phosphorus. *Nat. Commun.* **2014**, *5*, 4475.
- 737 (32) Terrones, H.; Lopez-Urias, F.; Terrones, M. Novel Hetero-
738 Layered Materials with Tunable Direct Band Gaps by Sandwiching
739 Different Metal Disulfides and Diselenides. *Sci. Rep.* **2013**, *3*, 1549.
- 740 (33) Tongay, S.; Zhou, J.; Ataca, C.; Lo, K.; Matthews, T. S.; Li, J.
741 B.; Grossman, J. C.; Wu, J. Q. Thermally Driven Crossover from
742 Indirect toward Direct Bandgap in 2D Semiconductors: MoSe₂ versus
743 MoS₂. *Nano Lett.* **2012**, *12*, 5576–5580.
- 744 (34) Datta, S. S.; Strachan, D. R.; Mele, E. J.; Johnson, A. T. C.
745 Surface Potentials and Layer Charge Distributions in Few-Layer
746 Graphene Films. *Nano Lett.* **2009**, *9*, 7–11.
- 747 (35) Gao, T.; Song, X. J.; Du, H. W.; Nie, Y. F.; Chen, Y. B.; Ji, Q.
748 Q.; Sun, J. Y.; Yang, Y. L.; Zhang, Y. F.; Liu, Z. F. Temperature-
749 Triggered Chemical Switching Growth of in-Plane and Vertically
750 Stacked Graphene-Boron Nitride Heterostructures. *Nat. Commun.*
751 **2015**, *6*, 6835.
- 752 (36) Hong, X. P.; Kim, J.; Shi, S. F.; Zhang, Y.; Jin, C. H.; Sun, Y. H.;
753 Tongay, S.; Wu, J. Q.; Zhang, Y. F.; Wang, F. Ultrafast Charge
754 Transfer in Atomically Thin MoS₂/WS₂ Heterostructures. *Nat.*
755 *Nanotechnol.* **2014**, *9*, 682–686.
- 756 (37) Kresse, G.; Joubert, D. From Ultrasoft Pseudopotentials to the
757 Projector Augmented-Wave Method. *Phys. Rev. B: Condens. Matter*
758 *Mater. Phys.* **1999**, *59*, 1758–1775.
- 759 (38) Blochl, P. E. Projector Augmented-Wave Method. *Phys. Rev. B:*
760 *Condens. Matter Mater. Phys.* **1994**, *50*, 17953–17979.
- 761 (39) Monkhorst, H. J.; Pack, J. D. Special Points for Brillouin-Zone
762 Integrations. *Phys. Rev. B* **1976**, *13*, 5188–5192.
- 763 (40) Dion, M.; Rydberg, H.; Schroder, E.; Langreth, D. C.;
764 Lundqvist, B. I. Van Der Waals Density Functional for General
765 Geometries. *Phys. Rev. Lett.* **2004**, *92*, 246401.
- 766 (41) Klimes, J.; Bowler, D. R.; Michaelides, A. Van Der Waals
767 Density Functionals Applied to Solids. *Phys. Rev. B: Condens. Matter*
768 *Mater. Phys.* **2011**, *83*, 195131.
- 769 (42) Hu, Z. X.; Lan, H. P.; Ji, W. Role of the Dispersion Force in
770 Modeling the Interfacial Properties of Molecule-Metal Interfaces:
771 Adsorption of Thiophene on Copper Surfaces. *Sci. Rep.* **2015**, *4*, 5036.
- 772 (43) Wu, J. B.; Hu, Z. X.; Zhang, X.; Han, W. P.; Lu, Y.; Shi, W.;
773 Qiao, X. F.; Ijias, M.; Milana, S.; Ji, W.; Ferrari, A. C.; Tan, P. H.
774 Interface Coupling in Twisted Multilayer Graphene by Resonant
775 Raman Spectroscopy of Layer Breathing Modes. *ACS Nano* **2015**, *9*,
776 7440–7449.